Supplementary Information

Salt Particle Suspension Electrolyte with Trace-Water for Improving Ionic Concentrations at Interfaces in Zinc-Based Dual-Ion Batteries

Yitao He[a,b,], Fafa Yu[a], Jiří Červenka[b,*]*

[a] *Department of New Energy Science and Engineering, School of Energy and Environment, Anhui University of Technology, Ma'anshan, China*

[b] *Department of Thin Films and Nanostructures, FZU – Institute of Physics of the Czech Academy of Sciences, Cukrovarnická 10/112, 162 00 Prague 6, Czech Republic*

Corresponding e-mail:

* Yitao He: yitao@fzu.cz

* Jiří Červenka: cervenka@fzu.cz

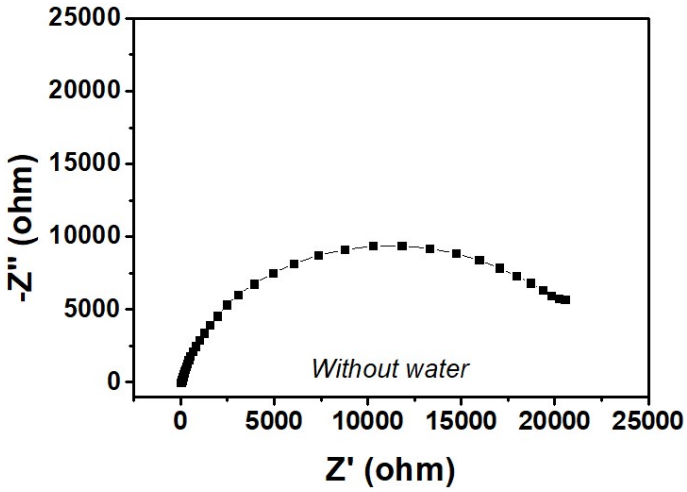

Figure S1. Nyquist plot of the battery using the electrolyte of 2M-SPSE without water.

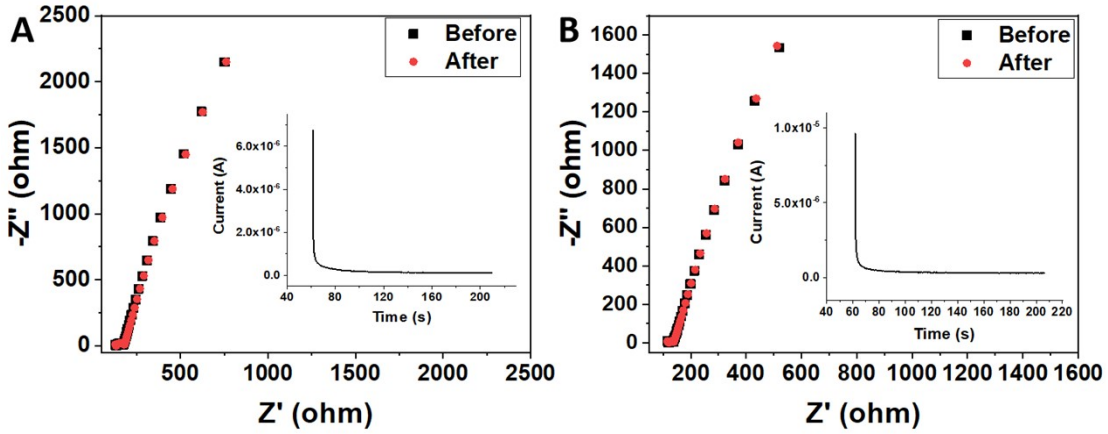

Figure S2. The EIS plots of (A) saturated DMC solution and (B) 2M-SPSE-30μL in the symmetrical EG||EG cells, before and after i-t tests under a certain potential (10 mV); and their corresponding i-t curves; *Before and after* means the EIS was measured before and after i-t curve tests, respectively.

We calculated the transference numbers of anion according to the equation:[1, 2]

$$t = \frac{I_s(\Delta V - I_i R_i)}{I_i(\Delta V - I_s R_s)} \quad \text{(S1)}$$

where t is the transference number; I_s is steady state current; I_i is initial current; R_s is steady state impedance; R_i is initial impedance; ΔV is a voltage perturbation (10 mV). It is important to note that the measured transference number inherently reflects contributions from both anions and cations. Therefore, the EG||EG symmetrical cell configuration was employed, thereby eliminating the influence of excess cation sources of Zn foil in the system. The impedance values were extracted from the EIS plot in **Figure S2**.

The measured parameters for two cells are:

Saturated DMC solution: I_s: 1.3089E-7 A; I_i: 6.75049E-6 A; R_s: 129.8 Ω; R_i: 132.2 Ω; t≈0.018.

2M-SPSE-30μL: I_s: 3.43231E-7 A; I_i: 9.63135E-6 A; R_s: 120.3 Ω; R_i: 119.6 Ω; t≈0.032.

The SPSE exhibits a higher anion contribution to the ionic current. Notably, the 2 M $Zn(OTf)_2$ in pure water electrolyte demonstrates an even larger transference number; however, the cell using it can not be charged successfully due to excessive water content. Consequently, the transference number alone cannot serve as a definitive metric for evaluating overall battery performance, but this parameter can probably complement other metrics (e.g., ionic conductivity, stability) to guide the optimization of electrolytes for specific applications.

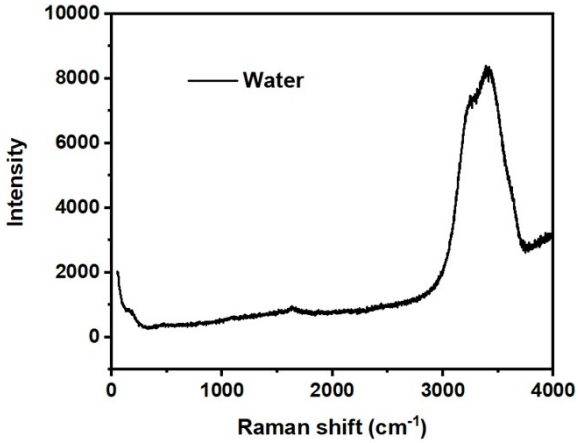

Figure S3. Raman spectroscopy of pure deionized water.

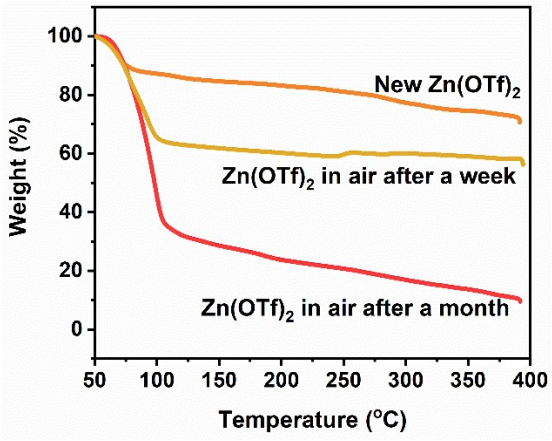

Figure S4. Thermogravimetric curves of $Zn(OTf)_2$ powders stored in the air for different times.

Based on thermogravimetric curves (**Figure S4**), the amount of adsorbed water in freshly opened commercial $Zn(OTf)_2$ containers was less than 10 wt.% and completely evaporated before the temperature reached 80°C. As the temperature increased, the $Zn(OTf)_2$ powder showed a slow weight loss due to the decomposition or oxidation reactions. However, storing the powder in the air for 1 week and 1 month caused the water content to reach 35 wt.% and 60 wt.%, respectively, distorting the actual concentration of the suspension electrolyte and reducing the cut-off voltage of the cell due to water splitting.

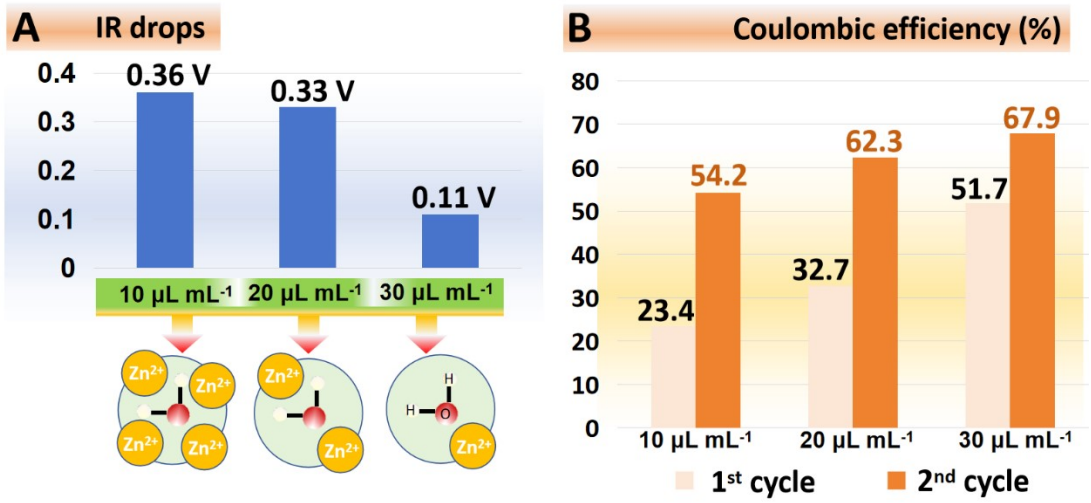

Figure S5. (A) The IR drops of the EG||Zn cells using 2 M suspension electrolytes (2M-SPSEs) with different trace water contents (10, 20 and 30 μL mL^{-1}) at 100 mA g^{-1} (insert: the coordination number ratio of one water molecule to Zn^{2+}) and (B) Coulombic efficiency (1st and 2nd cycles).

The IR drop values were determined by measuring the differences between the cut-off voltage and the actual discharge starting voltage observed in the discharge curves. The minimum IR drop was achieved when the coordination ratio of water molecules to Zn^{2+} was close to 1:1 (**Figure S5A**), and the initial Coulombic efficiency of the cell reached the highest value (**Figure S5B**), which was beneficial for enhancing cycle life and specific capacity. After several cycles, the Coulombic efficiency of the cell increased to more than 70 % and remained stable.

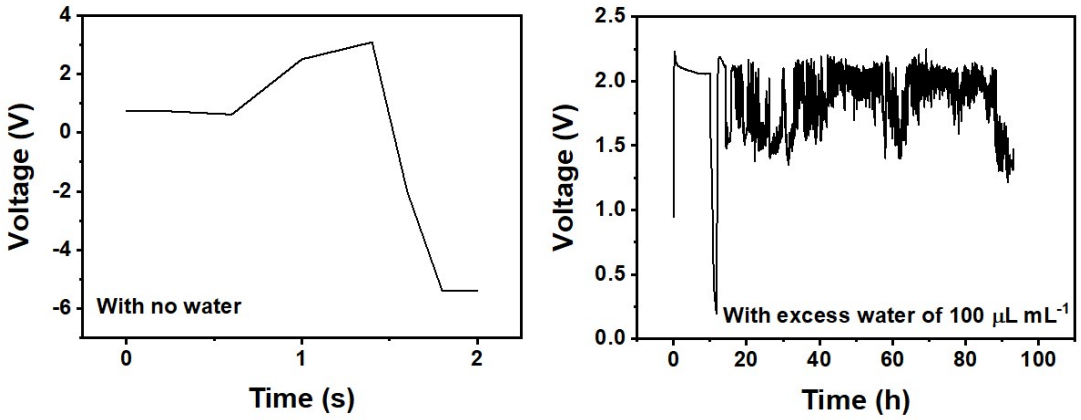

Figure S6. The charge-discharge curves of the batteries using the 2M-SPSEs with no water and excess water.

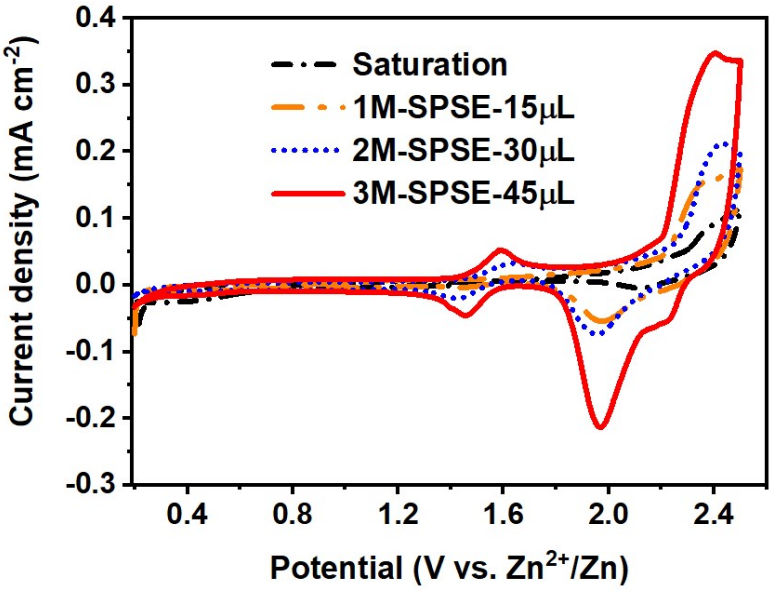

Figure S7. Cyclic voltammetry (CV) curves of EG||Zn dual-ion batteries assembled with electrolytes of different concentrations.

The CV curves of EG||Zn dual-ion batteries assembled with electrolytes of different concentrations are shown in **Figure S7**, with a scan rate of 0.5 mV s^{-1}. The saturated electrolyte resulted in the limited intercalation/de-intercalation of anions at the graphite cathode, while 1M-SPSE-15μL significantly enhanced anion activity. The intensity of oxidation-reduction peaks (i.e., the intercalation peak at 2.4 V and the de-intercalation peak at 2.0 V) was further enhanced with higher concentrations of the main salt.

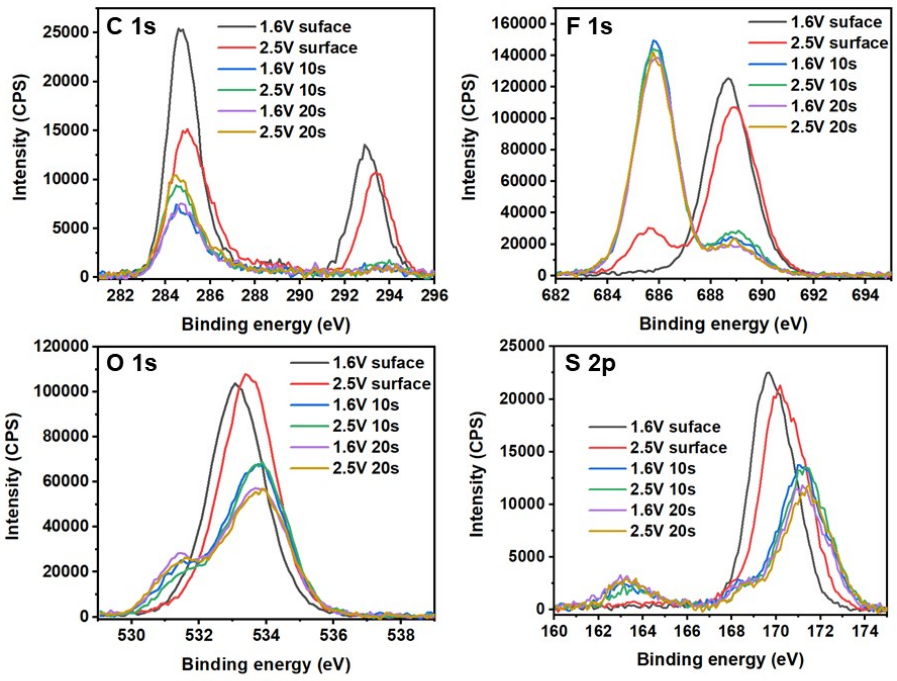

Figure S8. XPS spectra of the EG electrodes in 2M-SPSE-30μL after 10 cycles and potentiostatic

charging at 1.6 or 2.5 V.

The EG||Zn cells were assembled and cycled in the 2M-SPSE-30μL. After 10 cycles, one cell was charged to 1.6 V and kept potentiostatically at 1.6 V. Meanwhile, another cell was charged to 2.5 V and potentiostatically kept at 2.5 V for 10 h. Subsequently, the cells were disassembled, and the EG electrode sheets were removed without damage and tested by XPS after washing with DMC. The peak position difference between the XPS spectra at 1.6 and 2.5 V before etching can be attributed to the OTf^- adsorption capacity difference. A high voltage can promote more anion migration to the cathode surface. The F 1s and S 2p spectra indicate that the spectra of 1.6 V and 2.5 V samples showed little change, regardless of the etching time, indicating that the types of intercalated anions containing F and S atoms at both voltages are the same.

After etching, the C 1s spectra of the samples charged at 2.5 V are more intense and their peak positions are at higher binding energy than those at 1.6 V. The O 1s peak at 531.4 eV of the 1.6 V sample exhibits larger than that of the 2.5 V sample due to the presence of more C−O−C or C−O bonds. Therefore, the electrochemical oxidation of graphic carbon in the inner layer more easily occurs at 1.6 V. This type of electrochemical reaction with high reversibility can provide a large specific capacity, but it dramatically decreases the Coulombic efficiency.

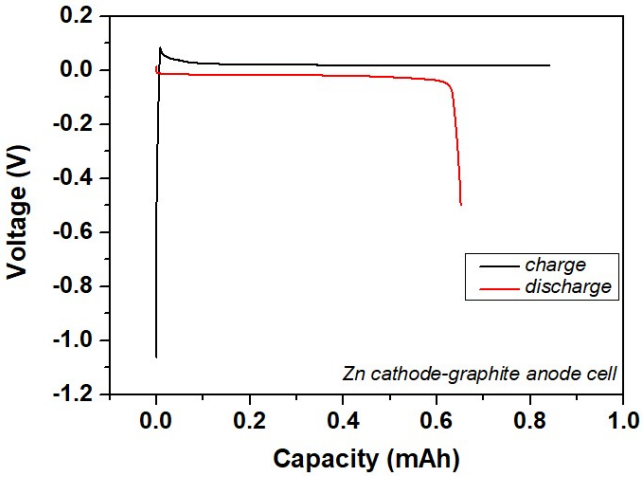

Figure S9. The first charge and discharge cycle in Zn||graphite cell with the 2M-SPSE-30μL.

In the Zn||graphite cell, a Zn foil was used as the positive electrode, and graphite was used as the negative electrode. The measurement conditions were set to a current density of 50 mA g^{-1} according to the mass of graphite active material on Cu foil; the low cut-off voltage was -0.5 V; and the charge time was 10 hours.

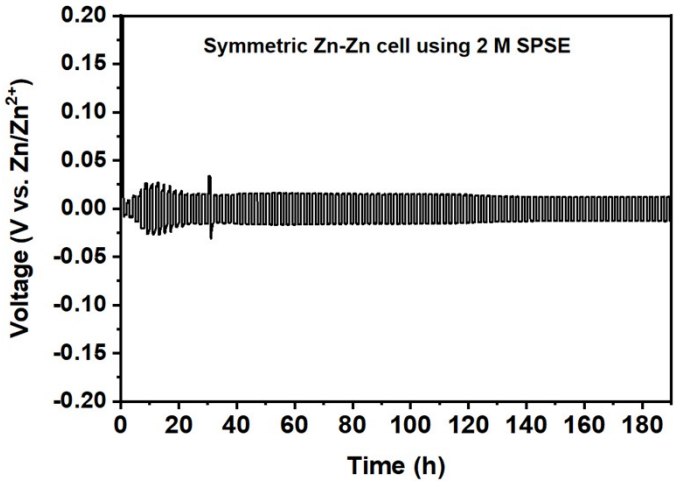

Figure S10. Stability performance of symmetric Zn-Zn cell using 2M-SPSE-30µL.

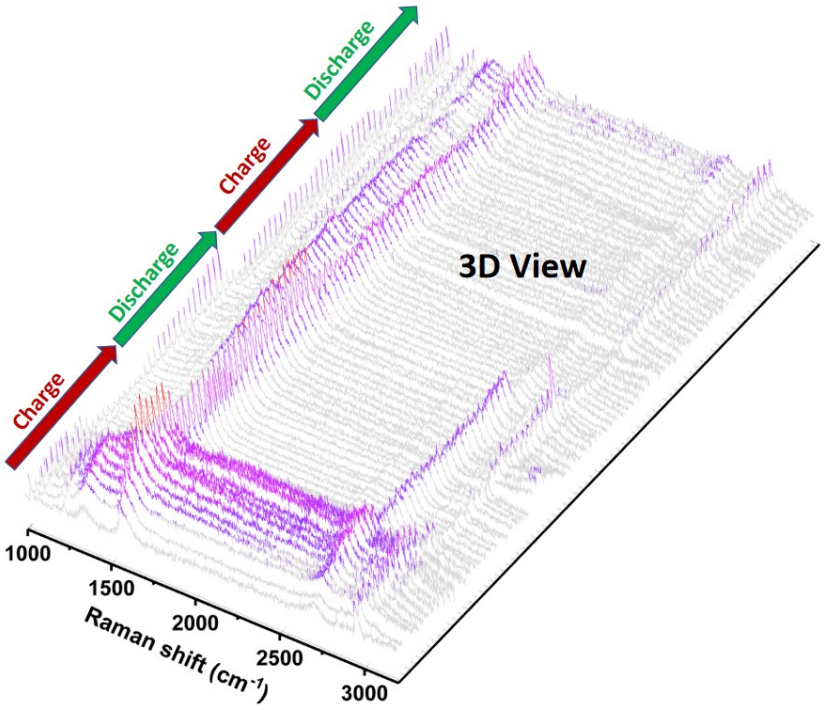

Figure S11. The 3D view presenting a series of in-situ Raman spectra for the first and second charging and discharging cycles (0.2 to 2.5 V) of the EG electrode within an EG||Zn cell, utilizing 2M-SPSE-30µL.

The D peak of EG was located at 1350.8 cm^{-1} and remained unchanged in the first and second cycles, as it is primarily induced by the edges of graphite flakes and is unrelated to graphite structure damage caused by electrochemical reactions. Another prominent characteristic peak representing graphite defects is located around 2970 cm^{-1}. This peak significantly weakened when anions intercalated but returned to its initial intensity after complete discharge, similar to phenomena reported in the literature.[3]

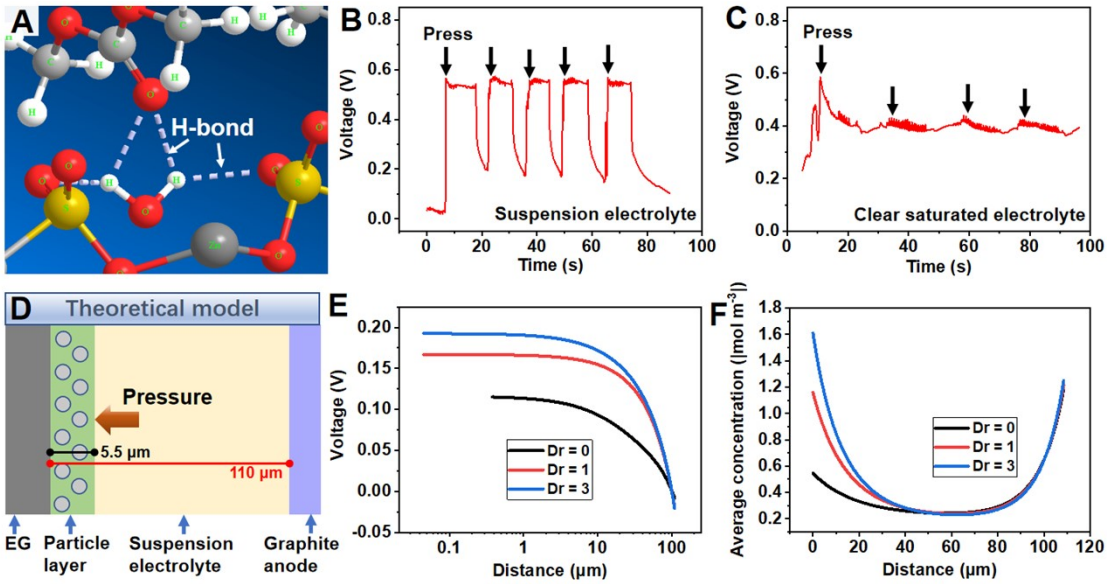

Figure S12. (a) Simulation of the hydrogen-bond in suspension $Zn(OTf)_2$ particles layer in DMC; (b) The open circle potential test of coin cell using 2M-SPSE-30μL with/without pressure; (c) The open circle potential test of coin cell using saturated electrolyte with/without pressure; (d) Scheme of the theoretical model that is used to simulate the influence of the piezoelectricity of the suspension particle layer on EG surface on the potential and concentration distribution in the coin cell; The simulated (e) OCP and (f) concentration distribution between the EG and graphite anode in the coin cells (the symbol D_r represents the remanent electric displacement (C m^{-2}) along with the *x* direction).

Figure S12A illustrates the abundant presence of hydrogen bonds in the $Zn(OTf)_2$ particle layer in DMC with trace amounts of water. This abundance of hydrogen bonds enhances the polarizability of the particle layer, leading to increased high-voltage tolerance and the acquisition of a piezoelectricity-like property. To investigate this phenomenon further, an EG||Zn dual-ion coin cell was assembled, and the open circle potential (OCP) was measured under an assembly pressure of 50 kg cm^{-2} every 5−10 s. The OCP results (**Figure S12B**) demonstrate an increase in the potential of the coin cell after the application of pressure when using a suspension electrolyte. In contrast, when using a clear saturated electrolyte without suspension particles, the OCP remains uncharged (**Figure S12C**). To explore the influence of the piezoelectricity of particle layer on the OCP and concentration distribution within the coin cell, a theoretical model was constructed using the COMSOL software (**Figure S12D**). The simulation considered an internal distance of 100 μm between the cathode and anode. The simulation results (**Figure S12E and S12F**) revealed an increasing potential difference between the cathode and anode, accompanied by a significant concentration increase near the cathode with an increasing D_r value. These findings indicate that the assembly pressure applied to the coin cell facilitates the accumulation of anions near the cathode, enhancing the OCP due to the presence of the suspension particle layer. Consequently, this phenomenon aids in preventing concentration polarization and improving the cut-off voltage of DIBs.

Table S1. Comparison of electrochemical performances of pure organic or aqueous zinc-based DIBs, zinc-ion batteries and this work

No.	Type of electrolyte	Used electrodes	Specific capacity (mAh g^{-1})	Retention (%) and lifespan	References
1	2 M suspension electrolyte with trace water	EG||graphite	178.66 at 10 mA g^{-1}; 77.23 at 100 mA g^{-1}; 304.8 Wh kg^{-1}; ≥ 2.0 V plateaus	84.7 % after 240 cycles at 100 mA g^{-1}	This work
2	6 M LiTFSI EC/DMC (Organic)	Carbon block||Al	270.2 Wh kg^{-1}	69.4 mAh g^{-1} after 350 cycles at 400 mA g^{-1}	4
3	3.5 M $Ca(FSI)_2$ EC/PC/DMC/EMC (Organic)	Graphite||PTCDA	75.4 at 100 mA g^{-1}	84.7 % after 350 cycles at 100 mA g^{-1}	5
4	0.8 M KPF_6 in EC:DEC (Organic)	KS6||graphite	54.6 at 100 mA g^{-1}	50.5 mAh g^{-1} after 400 cycles at 100 mA g^{-1}	6
5	0.8 M $NaPF_6$ in PC (Organic)	Graphite||hard carbon	52.0 at 100 mA g^{-1}	92.4 % after 250 cycles at 186 mA g^{-1}	7
6	1 M $LiPF_6$ in EC: DMC (Organic)	Graphite||Li	60.0 at 100 mA g^{-1}	100 cycles	8
7	21 M LiTFSI + 3 M $Zn(TfO)_2$ aqueous electrolyte	Graphite||Zn	70 at 20 mA g^{-1}	23 mAh g^{-1}, 600 cycles at 100 mA g^{-1}	9
8	1.2 M $Zn(TFSI)_2$ in acetonitrile (Organic)	Graphite||Zn	52 at 4 C	47 mAh g^{-1}, 1000 cycles at 100 C	10
9	30 M $ZnCl_2$ aqueous electrolyte	Zn-insertion Prussian blue||ferrocene/carbon	106 at 106 mA g^{-1}	80 % after 100 cycles at 106 mA g^{-1}	11
10	7 M $HClO_4$, 7 M H_2SO_4 aqueous electrolyte	Graphite||Zn	57, 61 at 100 mA g^{-1}	96.5 %, 72.9 % after 200 cycles at 200 mA g^{-1}	12
11	2 M $ZnSO_4$ aqueous electrolyte	PANI-V_2O_5||Zn	~200 at 0.5 A g^{-1} but ~1.0 V plateaus	55% after 200 cycles at 1 A g^{-1}	13
12	0.3 M $Zn(TFSI)_2$ in PC (Organic)	PANI||Zn	148 at 1 C, >1.2 V plateaus	\	14

13	2 M $ZnSO_4$ aqueous electrolyte	V_2O_5||Zn	175.4 at 0.5 A g^{-1}	16.2 mAh g^{-1} after 500 cycles	15
14	1 M $ZnSO_4$ and 0.05 M $MnSO_4$ aqueous electrolyte	ZMO@$Ti_3C_2T_x$ cathode	172.6 at 0.1 A g^{-1}, >1.6 V plateaus	\	16
15	1 M $ZnSO_4$ and 0.05 M $MnSO_4$ aqueous electrolyte	$ZnMn_2O_4$/N-doped graphene nanocomposite||Zn	221 at 100 mA g^{-1}; 1.4-1.5 V plateaus	\	17
16	2 M Zn(OTf)2 aqueous electrolyte	Graphene-PANI||Zn	184.5 at 0.2 A g^{-1}; ~1.0 V plateaus	\	18

Simulations

The module of Tertiary Current Distribution was applied to introduce the Nernst-Planck equation to describe the ion transport in the COMSOL software using the module of Electric Currents to simulate the electric field distribution. In order to compare the results under different conditions, four square regions have been constructed (**Figure S13**). In each square region, the narrow rectangle on the left represents the EG electrode. The circles represent the undissolved suspended $Zn(OTf)_2$ particles. The large square area on the right, except for the circle, represents the liquid DMC electrolyte, and the concentration was set to 0.2 M (the actual concentration of the saturated DMC solution). The mesh used in the model consists of Size and Boundary Layers.

Settings in Size:
Calibrate for: General physics;
Element size Parameters: Maximum element size 0.288 μm;
Settings in Boundary Layers:
Handing of sharp corners: Splitting;
Minimum angle for splitting and Maximum angle per split were default values;
Smooth transition to interior mesh: Number of iterations 4 and maximum element depth to process 6.

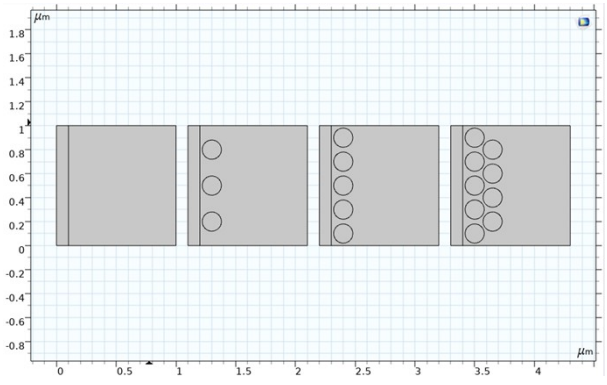

Figure S13. The geometrical model in the COMSOL software.

To simulate the electrodeposition process, the module of Tertiary Current Distribution was used for introducing the Nernst-Planck equation to describe the ion transport phenomenon:

$$\mathbf{J}_i = -D_i \nabla c_i - z_i u_{m,i} F c_i \nabla \Phi_l \quad \text{(S2)}$$

• c_i represents the concentration of the ion i (SI unit: mol m^{-3}),

• z_i is chemical valence,

• D_i is the diffusion coefficient (SI unit: $m^2\ s^{-1}$),

• $u_{m,i}$ is mobility (SI unit: s·mol kg^{-1}),

• F denotes the Faraday constant (SI unit: C mol^{-1}),

• Φ_l is the electrolyte potential,

• **u** is the velocity vector (SI unit: m s^{-1}),

• $\mathbf{J}_i$ denotes the molar flux relative to the convective transport.

Table S2. Detailed model parameters

Description	Value
Initial concentration of OTf^- in electrolyte	0.2 mol L^{-1}
Initial concentration of OTf^- in the circles	2 mol L^{-1}
Average current density on electrode surface	1 mA cm^{-2}
Initial potential	0.8 V
Ionic current density of suspended particle when dissolving	0.01 mA cm^{-2} (a reasonable arbitrary value)
Temperature T	293.15 K
Stoichiometric coefficient of anion	1

References

1. I. Kim, S. Jang, K. H. Lee, Y. Tak and G. Lee, *Energy Storage Materials*, 2021, **40**, 229-238.

2. Z. Yu, S. Jiao, S. Li, X. Chen, W.-L. Song, T. Teng, J. Tu, H.-S. Chen, G. Zhang and D.-N. Fang, *Advanced Functional Materials*, 2019, **29**, 1806799.

3. B. S. Elman, M. S. Dresselhaus, G. Dresselhaus, E. W. Maby and H. Mazurek, *Phys. Rev. B*, 1981, **24**, 1027-1034.

4. W. Huang, B. Meng, J. Li, K. Yang and Z. Fang, *ACS Appl. Energy Mater.*, 2022, **5**, 14487-14495.

5. J. Li, C. Han, X. Ou and Y. Tang, *Angew. Chem. Int. Ed.*, 2022, **61**, e202116668.

6. J. Zhu, Y. Li, B. Yang, L. Liu, J. Li, X. Yan and D. He, *Small*, 2018, **14**, e1801836.

7. Z. Hu, Q. Liu, K. Zhang, L. Zhou, L. Li, M. Chen, Z. Tao, Y. M. Kang, L. Mai, S. L. Chou, J. Chen and S. X. Dou, *ACS Appl Mater Interfaces*, 2018, **10**, 35978-35983.

8. B. Pattavathi, V. Surendran, S. Palani and M. M. Shaijumon, *Journal of Energy Storage*, 2023, **68**, 107878.

9. H. Zhang, X. Liu, B. S. Qin and S. Passerini, *Journal of Power Sources*, 2020, **449**, 227594.

10. Z. Chen, T. M. Liu, Z. M. Zhao, Z. H. Zhang, X. Q. Han, P. X. Han, J. D. Li, J. Z. Wang, J. J. Li, S. Q. Huang, X. H. Zhou, J. W. Zhao and G. L. Cui, *Journal of Power Sources*, 2020, **457**, 227994.

11. X. Wu, Y. Xu, C. Zhang, D. P. Leonard, A. Markir, J. Lu and X. Ji, *J Am Chem Soc*, 2019, **141**, 6338-6344.

12. Y. Zheng, X. Xie, H. Ueno, T. Deng and W. Zheng, *Advanced Energy Materials*, 2024, **14**, 2401914.

13. Y. Zhang, C. Peng, Y. Zhang, S. Yang, Z. Zeng, X. Zhang, L. Qie, L.-L. Zhang and Z. Wang, *Chemical Engineering Journal*, 2022, **448**, 137653.

14. A. Guerfi, J. Trottier, I. Boyano, I. De Meatza, J. A. Blazquez, S. Brewer, K. S. Ryder, A. Vijh and K. Zaghib, *Journal of Power Sources*, 2014, **248**, 1099-1104.

15. X. Sun, X. Lv, M. Zhang, K. Shi, Z. Li, X. Pan, T. Lian, R. Chen, F. Wu and L. Li, *ACS Nano*, 2024, **18**, 8452-8462.

16. M. Shi, B. Wang, Y. Shen, J. Jiang, W. Zhu, Y. Su, M. Narayanasamy, S. Angaiah, C.

Yan and Q. Peng, *Chemical Engineering Journal*, 2020, **399**, 125627.

17. L. Chen, Z. Yang, H. Qin, X. Zeng and J. Meng, *Journal of Power Sources*, 2019, **425**, 162-169.

18. X. Liao, C. Pan, H. Yan, Y. Zhu, Y. Pan and C. Yin, *Chemical Engineering Journal*, 2022, **440**, 135930.